Catalysis Today 210 (2013) 124–134

Contents lists available at SciVerse ScienceDirect

Catalysis Today

journal homepage: www.elsevier.com/locate/cattod

Ni based oxygen carrier over γ-Al_2O_3 for chemical looping combustion: Effect of preparation method on metal support interaction

Mohammad R. Quddus [a], Mohammad M. Hossain [b], Hugo I. de Lasa [a,*]

[a] The University of Western Ontario, London, ON, Canada N6A 5B9
[b] King Fahd University of Petroleum & Minerals, Saudi Arabia

ARTICLE INFO

Article history:
Received 31 August 2012
Received in revised form 8 February 2013
Accepted 9 February 2013
Available online 29 March 2013

Keywords:
CO_2 capture
CLC
Nickel-based oxygen carrier
Metal–support interaction

ABSTRACT

This study deals with the development of a Ni based oxygen carrier (OC) over La-modified and Co-doped γ-Al_2O_3 suitable for a fluidized bed chemical-looping combustion (CLC) process. La is found to stabilize the bulk phase transformation of γ-Al_2O_3 whereas Co minimizes the formation of irreducible bulk nickel aluminate. Apart from these beneficial effects, the reducibility and the structural properties of the prepared OCs are found to be modified by the different preparation methods used. The N_2 adsorption isotherm shows that γ-Al_2O_3 retains its structural integrity in only one preparation method. Reducibility as determined by consecutive temperature programmed reduction and oxidation techniques resembles the chemical properties of δ- and θ-Al_2O_3 for the other two preparation methods. However, no bulk phase change is detected for the three OCs using XRD. This suggests that the observed changes occur mainly at the molecularly thin surface layers of the OCs which display structural properties (geometric, electronic, coordination) significantly different from those of the bulk. The prepared OCs are also tested under CLC operating condition of the Chemical Reactor Engineering Center (CREC) fluidized Riser Simulator, using multiple reduction/oxidation cycles. Reactivity results obtained show expected reducibility, oxygen carrying capacity and stability with the three different preparation techniques.

1. Introduction

Carbon dioxide (CO_2) is regarded as one of the most prevalent greenhouse gases contributing to the global warming. The concentration of CO_2 in the atmosphere has increased significantly over the past few decades as a result of the dependency on the fossil based fuels for energy production. Thus, simultaneous power generation through combustion of fossil based fuels and efficient capture of CO_2 has been recognized as a promising choice for reducing CO_2 emissions significantly. However, although most of the available technologies can reduce CO_2 emissions, they are also accompanied by high energy penalty, thus reduce energy efficiency of the processes and increase the price of the energy [1]. In this regard, chemical-looping combustion (CLC) appears to have the potential of delivering a most efficient technology for CO_2 capture with significantly reduced economic cost [2]. As a consequence, during the past few years, CLC has received growing attention as an energy efficient CO_2 capture technology for power generation.

CLC, a reversible combustion method [3,4], typically employs a dual fluidized bed system where a metal known as oxygen carrier (OC) is circulated between the two twin beds. The solid carrier in its oxide form provides the oxygen needed for combustion in the fuel reactor. The oxygen depleted solid material is then transferred to the regenerator (air reactor) for re-oxidation and recycled back to the fuel reactor completing in this manner the CLC "loop". The separation of fuel and air reactors avoids dilution of flue gas stream with nitrogen. Therefore, the flue gas is constituted primarily by carbon dioxide and water vapor. Condensation of the water vapor allows the separation of carbon dioxide without the need of an extra separation step and avoids energy penalty involved in downstream processing. Moreover, the total combustion enthalpy over the two steps is the same as the conventional combustion, where the fuel is burned in direct contact with oxygen from air. Furthermore, given that oxygen is supplied in CLC via a solid carrier; this eliminates the need for air in the fuel reactors. Thus, there is no nitrogen–oxygen contacting in the

* Corresponding author at: Chemical Reactor Engineering Center, Faculty of Engineering, Department of Chemical and Biochemical Engineering, The University of Western Ontario, London, ON, Canada N6A 5B9. Tel.: +1 519 661 2144; fax: +1 519 850 2931.
E-mail address: hdelasa@eng.uwo.ca (H.I. de Lasa).

0920-5861/$ – see front matter © 2013 Published by Elsevier B.V.
http://dx.doi.org/10.1016/j.cattod.2013.02.005

fuel reactor and as a result, no opportunity for nitrogen oxide formation [1,5].

However, the non-availability of suitable OCs still hinders the large-scale application of CLC. In this respect, a suitable OC should have (a) good fluidization properties, (b) high oxidation capacity with high reactivity for reduction reactions, (c) favorable thermodynamics regarding the complete fuel conversion to CO_2 and H_2O, (d) limited cost and be environmental friendly, and (e) be resistant to attrition and agglomeration [1]. To this end, more than 700 carriers (e.g. supported and unsupported metal, mixed metal, synthetic materials, minerals and waste materials) have been considered and tested under strict CLC conditions. Recent reviews summarizing the characteristics of available carriers were published by Hossain and de Lasa [5] and Adanez et al. [1].

Ni based OC have been studied most extensively due to its superior reactivity, negligible volatility at high operating temperature of CLC and near complete conversion of CH_4. Supported nickel has received a great deal of attention given its favorable fluidization properties and resistance to agglomeration and attrition. Among various supports (ZrO_2, Al_2O_3, YSZ, SiO_2, etc.) Ni over α-Al_2O_3 was reported to be the most suitable one for this high temperature operation [6–10]. However, at this operating condition Ni also tends to react strongly with support and forms irreducible solid solution like $NiAl_2O_4$ spinel. This strong metal support interaction results in reduced reactivity and oxygen carrying capacity of the OC. Bimetallic carriers were found favorable to reduce the strong interactions or to minimize the formation of this solid solution, thus enhanced reactivity as reported by several others [11,12]. An example of this is the case of Ni over α-Al_2O_3 with small amount of added Co. Co has important affinity to interact with Al_2O_3 forms cobalt aluminate.

Thus, replacing a relatively small fraction of nickel by an equivalent amount of cobalt appears to help minimizing the undesirable formation of nickel aluminate. Nonetheless, low surface area of α-Al_2O_3 accommodates large Ni crystallites and reduced the maximum possible oxygen carrying capacity based on the amount of metal loaded. Thus, high surface support like γ-Al_2O_3 has drawn significant attention. This high surface area assists in the production of a highly dispersed Ni crystallite with increased oxygen carrying capacity. However, at the CLC operating condition, γ-Al_2O_3 is not thermally stable and formed mostly irreducible $NiAl_2O_4$. Hossain et al. [13,14] reported that the addition of La could not only help to thermally stabilize the γ-Al_2O_3, but also preserve its porous structure facilitating high dispersion of Ni crystallites, oxygen carrying capacity and reactivity. Apart from stabilizing the textural properties, the addition of La strengthens CO_2 adsorption on support, improves resistance to coking, retards metal sintering and thus enhances the stability of Ni based catalysts [15–17].

From the discussion above, this contribution considers fluidizable mixed metallic Ni-Co-La/γ-Al_2O_3 OCs for CLC. 20% Ni based OC was prepared in three different preparation methods over 5% La modified 1% Co doped γ-Al_2O_3. The morphology of the OC was assessed by using a N_2 adsorption isotherm and XRD analysis. Temperature programmed reduction (TPR) and oxidation (TPO) were used to determine the reducibility and oxygen carrying capacity of the prepared OC. The OC thermal stability was also determined in terms of metal dispersion and metal crystal size using H_2 pulse chemisorption in between every TPR and TPO cycle. The suitability of the OC was also confirmed under fluidized bed conditions in a CREC Riser Simulator. These conditions are close to the ones in CLC twin fluidized bed units where a fossil fuel like CH_4 is used for reduction and air is used for oxidation. All these characterization techniques also revealed that apart from the beneficial effect of La and Co addition, the reactivity and stability of the oxygen carries were influenced considerably by different preparation methods.

2. Experimental

2.1. Oxygen carrier preparation

In this study, the OCs were prepared using an "*incipient wetness*" technique under vacuum conditions. 100 μm of γ-Al_2O_3 (Sasol PURALOX/CATALOX SCCa Series: 98 wt% Al_2O_3, 0.002 wt% Na_2O, 0.01% Fe_2O_3, 0.015% TiO_2, 0.015% SiO_2 and LOI 2%) particles with 193 m^2/g specific surface area were used as the support. In order to improve the thermal stability, the alumina support was modified with 5 wt% La. The alumina support was later doped with 1 wt% Co to enhance the reducibility. On completion of these steps, 20 wt% nickel was added on the modified alumina support. With the aim of maximizing the oxygen carrying capacity, 20 wt% of Ni was selected as the highest loading limit [11,13,14]. The Ni utilization was very poor for the incremental addition above 25 wt% due to metal sintering or agglomeration [18].

Four main steps were involved in OC preparation: (a) support impregnation, (b) drying, (c) reduction and (d) calcination. The impregnation step was carried out in a quartz conical flask with a lateral outlet, which was connected to a 250 mmHg vacuum system. In each batch, 20 g of γ-Al_2O_3 was added into the conical flask and its inlet was sealed with a rubber septum to maintain vacuum conditions throughout the impregnation process. The vacuum was applied to remove the gases trapped inside the alumina support before impregnation. Meanwhile, 99.99% pure $La(NO_3)_3{\cdot}6H_2O$ (CAS 10277-43-7), $Co(NO_3)_2{\cdot}6H_2O$ (CAS 10026-22-9) and/or $Ni(NO_3)_2{\cdot}6H_2O$ (CAS 13478-00-7) received from Sigma–Aldrich was used as a precursors for the desired metal loading. The solution was prepared by dissolving a desired amount of the nitrate in distilled water. Based on the total pore volume of γ-Al_2O_3 measured using N_2 adsorption isotherm experiments, 0.5 mL water was used per gm of support. The prepared nitrate solution was introduced drop-by-drop, contacting the support under vacuum and continuous mixing conditions. The resulting paste was then dried slowly in a furnace with a temperature ramp of 0.5 °C/min increasing from ambient to 140 °C. Before returning to the ambient condition, the sample was kept at this temperature for an additional period of 4 h. Once dried, the prepared OC material was placed in the specially designed fluidized bed reactor. A gas mixture of 10% hydrogen with helium being the balance was flown through the particle bed in order to achieve fluidization. The bed temperature was then raised from ambient to 750 °C over 4 h and held constant at 750 °C for 8 additional hours. The main drawback of the incipient wetness pore volume impregnation technique is the limited amount of NiO that can be introduced into the support in each stage. In each cycle 5 wt% Ni was added to the modified support. Thus, these three steps, impregnation, drying and reduction were repeated until the desired metal loading was reached. On completion of the desired metal loading, the OC was calcined in an oven under an air flow at 750 °C using the same temperature ramp employed for the reduction.

Three OCs were prepared in this study by altering only the flow rate of the reducing gases. At low space velocity (15 h^{-1}), the particles resembled almost the fixed bed condition. As the velocity increased to 40 h^{-1}, the particles reached near minimum or minimum fluidization condition. The last OC was prepared at bubbling fluidized bed conditions with very high space velocity close to 300 h^{-1}. Thus, based on the particle bed condition, the OCs were named as HMF (half of gas flow rate required for minimum fluidization), MF (gas flow rate for minimum fluidization) and BF (gas flow rate for bubbling bed fluidization).

2.2. N_2 adsorption

Nitrogen adsorption measurements were carried out at 77 K on an ASAP 2010 automatic adsorption analyzer equipped with the micropore options from Micromeritics. Before the measurements, samples weighing from 0.1 to 0.2 g were placed in the degas port of the adsorption apparatus and degassed at 200 °C until the pressure reached below 5 mm Hg. Adsorption isotherms were measured under the relative pressure (P/P_0) range, based on the saturation vapor pressure, from $\sim 10^{-6}$ to 1.

2.3. Temperature programmed studies

Temperature programmed studies (TPR, TPO and H_2 pulse chemisorption) were performed using a Micromeritics AutoChem II 2920 Analyzer. An OC sample weighing 100–200 mg was placed in a U-shaped quartz reactor tube. This tube was then attached to the sample analysis port of the instrument, which is located inside a heating element. The specifics of the analyses for each of the temperature programmed studies are described in following subsections.

2.3.1. TPR/TPO

To perform the TPR test, a gas mixture containing 10% H_2 with the balance being Ar was circulated through a bed of the prepared OC particles at a rate of 50 mL/min. The temperature of the particle bed was raised from ambient to 950 °C at a rate of 10 °C/min, holding the temperature at 950 °C for an hour. The exit gas concentration was analyzed with a thermal conductivity detector (TCD) and further processed to calculate the amount of hydrogen consumed during the reduction process. This total amount of consumed H_2 was used to calculate the number of reducible species (W^{R}_{Ni}) and the percentage of metal reduction (f_R) as follows:

$$W^{R}_{Ni} = \frac{MW_{Ni} V_{H_2}}{\nu V_g} \quad (1)$$

$$f_R = \frac{W^{R}_{Ni}}{W^{a}_{Ni}} \times 100 \quad (2)$$

where MW_{Ni} represents the molecular weight of the reducible species (g), V_{H_2} stands for the volume of H_2 consumed at STP (cc), V_g denotes the gas molar volume at STP (cc/mol) and W^{a}_{Ni} is for the actual metal amount on the OC (g). ν stands for the stoichiometric number ('1') based on the following reaction stoichiometry: $NiO + H_2 \rightarrow Ni + H_2O$.

After the TPR experiment, H_2 pulse chemisorption was performed to determine the active metal surface area, the percent metal dispersion and the active particle size. Following chemisorption, TPO experiments were conducted. The steps for TPO were exactly the same as the ones for TPR with the exceptions that in this case, the flowing gas stream had a composition of 5% O_2 and 95% He and the bed temperature was increased up to 750 °C. As with the TPR, the total amount of consumed O_2 calculated from processed TCD data, was used to measure the number of oxidized species (W^{O}_{Ni}) and the percentage of metal oxidation (f_O) according to the following equation:

$$W^{O}_{Ni} = \frac{MW_{Ni} V_{O_2}}{\nu V_g} \quad (3)$$

$$f_O = \frac{W^{O}_{Ni}}{W^{a}_{Ni}} \times 100 \quad (4)$$

where V_{O_2} is the volume of H_2 consumed at STP (cc) and ν is equal to 0.5 based on the following reaction stoichiometry: $Ni + 0.5O_2 \rightarrow NiO$.

2.3.2. H_2 pulse chemisorption

Pulse chemisorption experiments were performed under a stream of argon gas flowing through a bed of pre-reduced carrier at a rate of 50 mL/min. A series of hydrogen pulses (1.0 mL) were injected at room temperature into the bed with a 1.5 min delay between each sequential injection. Each pulse generated a TCD peak which was recorded at the exit of the gas stream. Peak areas changed for each injection as a result of the H_2 chemisorbed amount. The pulse chemisorption experiment was discontinued when two consecutive TCD peaks had the same area. The total amount of chemisorbed H_2 on the active sites of the OC was determined from the processed TCD data and used to calculate the percent dispersion (D) as follows:

$$D = \frac{1017X}{Wf_R} \quad (5)$$

where X represents the total hydrogen chemisorbed ((mol of H_2/g of OC), W stands for the metal weight percentage and f_R denotes the fraction of reduced metal. Furthermore, the average crystal size (d_v in nm) is calculated as follows:

$$d_v = \frac{\varphi V_m}{S_m} \times \frac{1}{D} \quad (6)$$

where φ represents the particle shape constant, V_m stands for the volume of metal atoms (nm^3) and S_m denotes the average surface area (nm^2) of metal particles exposed per surface metal atom.

2.4. X-ray diffraction (XRD)

X-ray powder diffraction patterns were obtained on Rigaku Miniflex diffractometer using Ni filtered Cu Kα ($\lambda = 0.15406$ nm) radiation. A tube voltage of 40 kV and a tube current of 20 mA were used for each sample. The samples were scanned every 0.02° from 10° to 90° with scan time constant of 2°/min. Identification of the phase was made with the help of the Joint Committee on Powder Diffraction Standards (JCPDS) files. The crystallite sizes of NiO and Ni were calculated using Scherrer's equation:

$$d_{XRD} = \frac{0.9\lambda}{(\beta - \beta_0)\cos\theta} \quad (7)$$

where d_{XRD} is the volume average diameter of the crystallite (nm) and $(\beta - \beta_0)$ is the full width at half maxima of the peak.

2.5. Reactivity in the CREC Riser Simulator

The CREC Riser Simulator is a bench scale mini-fluidized bed reactor. This is an excellent tool for catalyst evaluation and kinetic studies at the expected turbulent fluidized bed conditions of an industrial scale fluidized CLC unit [19]. Thus, the reactivity, regenerability and stability of the prepared OCs were evaluated using this reactor under CLC operating conditions. The CREC Riser Simulator has an upper and lower shell between which the 55 cm^3 reactor (catalyst basket) is placed. Apart from acting as a heating element, this sectional arrangement of the shells allows easy loading and unloading of the OC from the reactor. The reactor is connected to a large vacuum box (1055 cm^3), which serves as an isolation chamber and separates the reactant gases from the solid carrier on completion of a reaction. The other important component of the Riser Simulator is the impeller, which is located just above the basket containing the solid particles. The impeller rotates at a very high speed (up to 7000 rpm) during the reaction and forces the reactant gases to flow outwardly from the impeller center and downwards later into the outer reactor annulus. Schematic diagram of the CREC-Riser Simulator, along with the gas injector port, is illustrated elsewhere [13]. The promoted flow pattern forces an

up-flow of the reactant gases through the catalyst basket and fluidizes the OC particles.

The reduction reactions were performed using 0.5 g of OC. The OC was loaded into the reactor basket and then placed in between the inconel reactor shells. The temperature of the system was raised to the desired 650 °C for the combustion cycle (carrier reduction) under argon flow ensuring an oxygen (air) free environment. Once the pre-set temperature was reached, the argon flow was discontinued. Simultaneously, the reactor was isolated from the vacuum box with the reactor pressure being set at 1 atm. Before the initiation of the reaction, the vacuum box was evacuated up to 1.0 psi using a vacuum pump. Once these desired conditions were met, the impeller was turned on and a feed (CH_4) was injected into the reactor using a preloaded syringe. During this period of methane combustion, the changes in the pressure profile of the reactor were recorded using a pressure transducer. A valve isolating the reactor and the vacuum box was opened at the end of the pre-specified reaction time (30 s). Almost all the contents of the reactor were transferred instantly to the vacuum box, given the pressure difference and the larger vacuum box volume. In addition, an abrupt decrease in the reactor pressure confirmed that most of the reactant/product species were transferred from the reactor to the vacuum box almost instantaneously. This way any reaction with the OC carrier after the pre-specified time was prevented. Finally, the product species were analyzed using a gas chromatograph and the CH_4 conversion was calculated as follows:

$$X_{CH_4} = \frac{C_{CO_2,out} + C_{CO,out}}{C_{CO_2,out} + C_{CO_2,out} + C_{CH_4,out}} \times 100 \quad (8)$$

Before the next cycle, the OC was regenerated (oxidized) by flowing air at a 550 °C temperature for at least 10 min to ensure complete oxidation.

3. Results and discussion

3.1. N_2 adsorption

The characteristics of porous material, namely specific surface area, pore size and pore size distribution, play an important role in determining the dispersion of the active sites, the adsorption capacity, reactivity and sintering probability of the OC. A large surface area facilitates high dispersion with increased adsorption capacity and reactivity [20]. The N_2 adsorption isotherm is widely used for accurate prediction of all these important properties and thus used in this study for evaluating the porous characteristics of the prepared OCs.

Fig. 1 reports the N_2 adsorption–desorption isotherms of all prepared OCs including the support itself. Several remarks can be drawn: (a) the shape of the isotherms is consistently of type IV profile [21], which is common for mesoporous solid and (b) there are significant differences in the structural properties of the various OCs under study.

Thus, it is apparent that the structural properties have been altered using different preparation methods. The volume of intake below $P/P_0 = 0.05$ decreases considerably for prepared OC as in the case of HMF. However, the changes are slight for BF suggesting that this preparation method allows the retention of pore structure of the support. This observation is also reinforced by the start of pore condensation phenomena at the same $P/P_0 = 0.55$ for both the support and BF. The pore condensation at higher relative pressure for both HMF and MF is indicative of the presence of larger pores. These larger pores might be resulting from pore blockage and from the collapse of small pores. Apart from these, all isotherms display type H1 [22] hysteresis loop which is associated with solid porous material consisting of well-defined cylindrical-like pore channels or agglomerates of compacts of approximately uniform sphere [23].

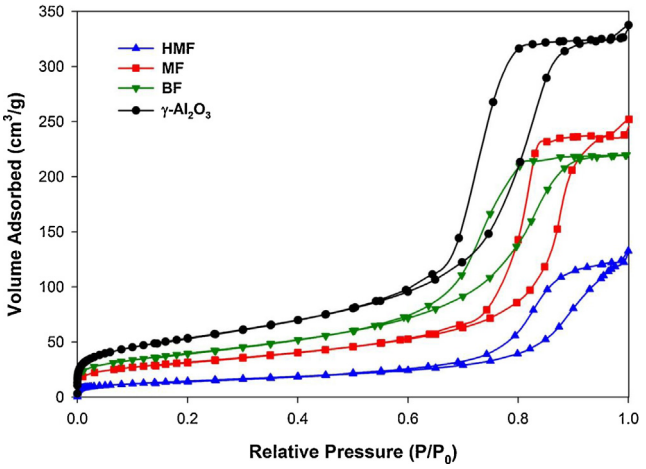

Fig. 1. N_2 adsorption–desorption isotherms of different OCs and support.

Moreover, the less steep hysteresis loop for sample HMF suggests the existence of wide range of pores compare to the others [23]. All these inferences have been numerically analyzed in the following section.

The BET equation was used to calculate the surface area. This was due to the linearity of the N_2 isotherm between the range of $P/P_0 = 0.05$–0.3 with a very small uptake of N_2 below a P/P_0 of 0.05. The results are summarized in Table 1. The values of "C" are found between 3 and 1000 [23] and less than 300 [20], which are acceptable for mesoporous solids. The experimental values of volume adsorbed (V_{ads}) for various OCs, which were obtained as a function of P/P_0, were also plotted against universal thickness of N_2 molecule in multilayer adsorption (t-plot). It is widely accepted that the presence of micropores results in a deviation from linearity between V_{ads} and t [23–25]. The linearity of the results through the origin in all three cases also serves as an evidence of the mesoporosity of the prepared OCs. Thus, it was expected that the t-plot area calculated from the slope should be analogous to the area determined using BET. This is apparent from the results in Table 1. The specific area obtained using these two methods also comply with the results calculated from pore size distribution (cumulative area (A_{cum}) in Table 1). The pore size distributions in all of these cases were done using the adsorption branch isotherm and plotted in Fig. 2. The conformity of A_{cum} with A_{BET} implies that the pore structure of the OCs are either cylindrical or of the ink-bottle type with

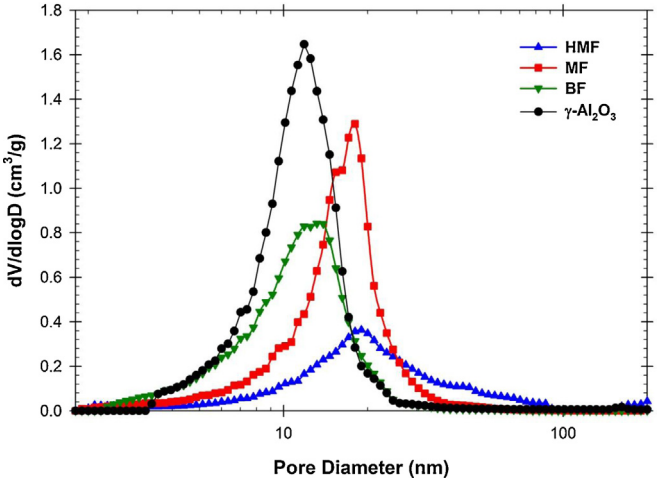

Fig. 2. Pore size distribution of different samples based on adsorption branch of the isotherm assuming cylindrical pore.

Table 1
Results of surface area, pore size and pore volume calculated by to different methods.

Sample ID	BET		*t*-plot		Pore size distribution			From isotherm	
	A_{BET} (m^2/g)	C	V_m (cm^3_{STP}/g)	$A_{t\text{-plot}}$ (m^2/g)	A_{Cum} (m^2/g)	V_p^{cum} (cm^3_{STP}/g)	d_{avg} (nm)	V_p (cm^3_{STP}/g)	d_{avg} (nm)
γ-Al_2O_3	193.39	98.88	44.42	193.75	197.84	0.5043	10.19	0.5034	10.42
HMF	52.87	76.78	12.14	53.07	51.30	0.1865	14.54	0.1833	13.97
MF	112.51	147.75	25.85	112.95	112.42	0.3650	12.98	0.3679	12.98
BF	142.38	113.07	32.71	142.93	144.39	0.3377	9.35	0.3396	9.53

narrow neck [26]. The average pore diameter (d_{avg}) with different OCs were calculated both from pore size distribution and N_2 isotherm and reported accordingly in Table 1 using the relation, $d_{avg} = 4\,V_p/A$.

The main challenge while preparing OC with Ni over γ-Al_2O_3 is to maintain the porous structure of the support as Ni facilitates the sintering of γ- to δ- to θ-Al_2O_3 (50–120 m^2/g) [27]. In contrast, La can act to reduce the extent of sintering and retard phase conversion by forming ultrastable solid solution like $LaAlO_3$ [13,27,28]. However, based on the results of Table 1 and Fig. 2, it is noticeable that the porous structure of γ-Al_2O_3 has been altered significantly. Though all the three OCs were prepared with the same amount of La, different preparation methods were found to influence the porous structure of the support. The Sample BF, which was prepared with the maximum gas flow rate, has the highest surface area (Table 1). The d_{avg} is slightly smaller than that one of the support.

Fig. 2 suggests that this preparation method preserved the structure of the support. As the flow rate decreased from BF to MF and HMF, the surface area decreased with increasing d_{avg} and a wider range of pore sizes. These structural changes were mainly caused by sintering process which could be leading to the phase transformation of γ- to δ- to θ-Al_2O_3. The effect of the gas flow rate on the sintering process can be explained by the exothermic decomposition of metal nitrate precursors in H_2 environment [18,29–31]. This decomposition process has been discussed extensively in Section 3.2. This exothermic process likely creates high localized temperature in the catalyst pellet and thus leads to metal sintering during the preparation steps. It is reported that methods like the one using diluted H_2 high space velocity with a slow temperature ramp and holding the sample at a certain temperature for an extended periods of time facilitate slow decomposition of nitrate salts. It is suggested that this approach prevents sintering [18,27].

Based on the discussion above, in case of sample BF, high gas flow rate minimizes the sintering effect by taking away the heat released during the metal nitrate decomposition steps, thus minimizing the high localized temperature in the support particles. High gas velocity is also favorable to ward off the water produced through these exothermic reactions. Failure to remove this water enhances the agglomeration of Ni crystal [18] leading to pore blockage of the support, and thus reduced surface area. This is why high surface area (Table 1) was observed with sample BF while preserving the porous structure (Fig. 2) of the support. This pore structure facilitated high dispersion of Ni crystals especially on the pore walls. D and crystal size (d_v and d_{XRD}) calculated using H_2 chemisorption experiment and XRD as reported in Table 2 also portrayed the same results. The available surface area and V_p of the pores shrunk as more Ni settled on the pore walls. As a consequence, few smaller pores appeared in the 2–4 nm ranges and d_{avg} dropped slightly from that of the support (calculated from both the pore size distribution and N_2 isotherm, Table 1). No pore blocking or breaking phenomena has been observed in case of BF. However, the f_O values reported in Table 2 suggest that almost 14% Ni could not contribute toward the oxygen carrying capacity. This might be due to the difficulty of accessing Ni metals buried under the layer of Ni in small pores. f_O represents the more reliable picture about the state of accessible Ni than f_R, which is almost 100% in this case, included the non-stoichiometric H_2 consumption by $NiAl_2O_4$ [12,32,33]. All these conclusions are visibly supported by Fig. 3(c), where the pore size distributions are reported after each successive metal loading.

On the other hand, sintering and crystal agglomeration processes are promoted with decreasing gas flow rates. In case of MF, the small pores collapsed to large ones. As a result, the support lost its surface area accounted for by small pores. However the total the pore volume increased (Fig. 3(b)). As the metal loadings continued, formation of large pores from the smaller ones stabilized and pore blocking initiated by large Ni crystals. The MF samples had both small Ni crystals on the wall and some large ones blocking the pores. However, these two effects reached their extreme with HMF. The total pore structure of the support disintegrated due to extreme sintering followed by pore blocking resulted in burial of considerable amount Ni metals. Ultimately, the support lost most of its surface area (Table 1), V_p with a wider range of large pores

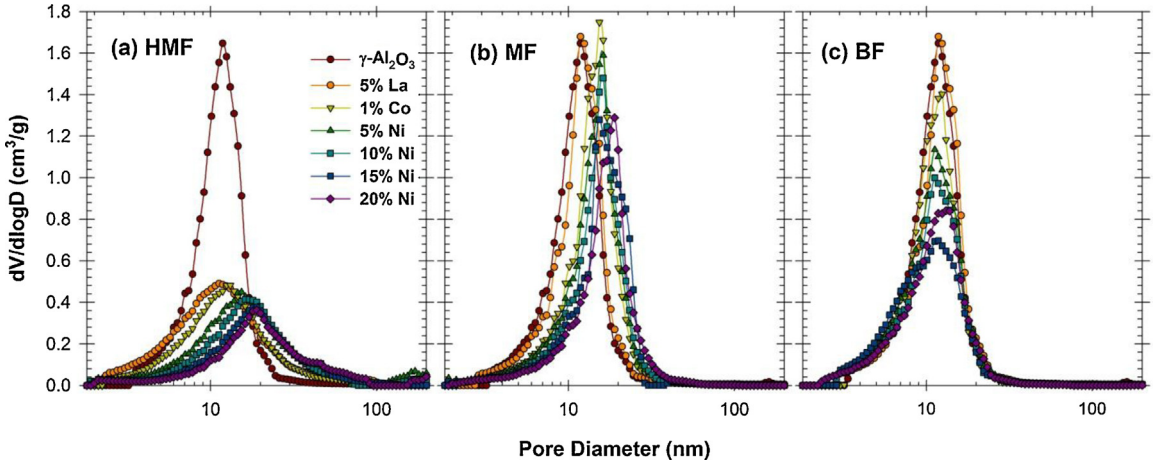

Fig. 3. Pore size distribution of different samples after each successive metal loading.

Table 2
Reactivity and stability parameters for different oxygen carriers.

Sample	Reduction f_R (%)	Reduction below 750 °C f_R^{750} (%)	Dispersion D (%)	Average crystal size d_v (nm)	Oxidation f_O (%)
HMF	86	78	1.69	58	78
MF	96	86	2.03	47	84
BF	98	76	3.83	26	86

(Figs. 2 and 3(a)) compare to the MF and BF samples. This resulted in the lowest f_O, f_R and D with largest crystal sizes as shown in Table 2.

The structural properties and chemical characterizations as discussed in this section and in Section 3.2 are suggestive of the possible phase transformation of γ-Al_2O_3 to the δ- and/or θ-phases in case of MF and HMF respectively. However, the bulk structure was still found to preserve the γ-characteristics as shown in Fig. 5. These contrary findings have been explained particularly in Section 3.3.

3.2. Temperature programmed studies

Reactivity and stability under repeated reduction–oxidation cycles are the most important characteristics of an OC in CLC. Sequential reduction–oxidation can reduce the OC's activity by means of strong metal–support interactions resulting in the formation of non-reducible species and agglomeration of nickel crystallites. Thus, to investigate these matters successive TPR and TPO experiments were carried out in this study. TPR/TPO studies are also very useful to establish the reducibility (the temperature at which the reduction occurs and the percentage of reduction) and the oxygen carrying capacity of the OC.

TPR profiles of the prepared OC samples are reported in Fig. 4. Quantification (reduction and oxidation percentage, dispersion, etc.) of TPR data are summarized in Table 2. The reduction profile of HMF shows a large wide asymmetric TPR peak ranging from 350 to 750 °C. On the other hand, two distinguished peaks are observed in reverse intensity for both the MF and BF samples within the same temperature range. One can also notice the extension of the TPR profiles in all the three cases above the 750 °C level. This is an indication of species having strong interactions with the OC support. These observations imply the existence of surface heterogeneity, in other words, more than one type of species contributes to the overall reduction process.

According to the literature [7,11,13,16,17,34–36], the peak in the 400–600 °C temperature range can be attributed to the reduction of Ni^{2+} in the bulk NiO phase with reducible species remaining at higher temperature being $NiAl_2O_4$. Using TPR and X-ray diffraction studies, Rynkowski et al. [37] concluded that the reduction of the NiO species in the amorphous phase occurs in the temperature range of 380– 690 °C.

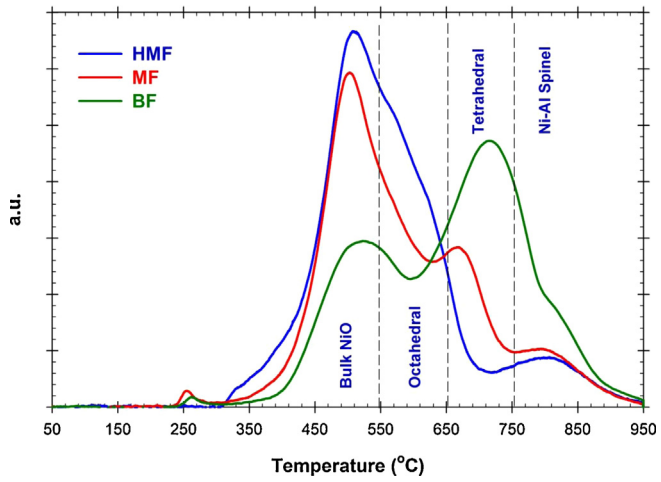

Fig. 4. TPR profiles of different oxygen carriers.

The reduction of $NiAl_2O_4$ spinel formed through strong metal support interaction occurs at temperatures above 780 °C. The high temperature range was narrowed down as surface (600–750 °C) and bulk (750–950 °C) $NiAl_2O_4$ [16]. Several others [38–40] reported that this surface aluminate is actually Ni^{2+} occupying the octahedral and tetrahedral sites of γ-Al_2O_3. Based on XRD, TPR and XPS analysis on γ- and κ-Al_2O_3 these authors showed that Ni^{2+} deposited on tetrahedral vacancies are mainly responsible for TPR peak above 650 °C. Lack of tetrahedral configurations in κ-Al_2O_3 resulted in two peaks below 650 °C which were assigned to bulk NiO and Ni^{2+} in octahedral spinel configuration. Similar conclusions were reported with Ni supported on different alumina phases (γ, γ + θ, θ + α, α) given their observed loss of surface hydroxyl groups [41]. Based on these literatures, the TPR profile could be sectioned according to Fig. 4 for four types of Ni^{2+} species over γ-Al_2O_3.

The only other possible species that can contribute to the TPR profiles are the oxides of La (La_2O_3 or $LaAlO_3$) and Co (CoO, Co_3O_4, $CoAl_2O_4$ or $NiCo_2O_4$). Hossain et al. [13,14] reported the possible existence of La as $LaAlO_3$ perovskite aluminate with the hydrogen consumed being negligible. It is believed that during the preparation steps La interacts with γ-Al_2O_3 to form $LaAlO_3$ perovskite aluminate or stays as amorphous La_2O_3. Both are difficult to reduce even at 950 °C [13,42].

In another study, Hossain et al. [8,11] also indicated that small amount (≤1 wt%) of Co stays mainly as stable $CoAl_2O_4$ over alumina rather than other oxide phases of Co. These authors along with Mattison et al. [43] reported that the reduction temperature for $CoAl_2O_4$ is higher than 800 °C. However, for such a small loading, the hydrogen consumption in $CoAl_2O_4$ is negligible as compared to the amount consumed by $NiAl_2O_4$. Nonetheless, the promotional effect of Co is apparent from all the three TPR profiles, as the amount of bulk $NiAl_2O_4$ formation is very low for such a loading of Ni over γ-Al_2O_3. This promotional effect can be assigned to the formation of oxidized Co species with $Al_2O_4^{2-}$ using the site-preference energy concept [11,12]. Thus, one can argue that use of a proper cobalt loading can minimize the formation of non-reducible species and provide a very reactive OC within the desired operating condition of CLC.

Based on the discussion above, it is apparent that the dissimilarity in the TPR profiles is mainly due the presences of varied concentration of Al^{3+} in tetrahedral configurations over γ-Al_2O_3. Even though all three materials are composed of the same amount of chemical compounds, preparation methods turned out to be the determining factor for NiO species interacting strongly with the support. Thus, it would be highly desirable to understand the chemistry involved in the preparation methods and the effect of controlling variable on the catalytic properties.

Decomposition and reduction of nitrate precursors in H_2 environment involve series of several exothermic and endothermic reactions steps. Based on thermal gravimetric analysis (TGA), differential thermal analysis (DTA) and chromatographic measurements, Bartholomew et al. [18] reported that the decomposition of nickel nitrate under H_2 environment resulted in reduced Ni directly

through the generation of NO, NO_2 and NH_3 as the product gas. Using TPR with a mass spectrometer, Jang et al. [44] showed that the decomposition of nickel nitrate may proceed simultaneously with the reduction and identified NH_3, N_2, NO, NO_2 and N_2O as the evolved gases. Out of these gases NO, NH_3 and N_2O were the most abundant. Furthermore, Yuvaraj et al. [45] suggests that the hydrogen reduction of transition metal nitrates may result in the formation of N_2, NH_3 or lower valent nitrogen oxides (NO_x).

The heat of reaction calculated and reported [18] for all these product gases are found highly exothermic (−86.5 to −267 kcal/mol) except for NO_2 which is slightly endothermic. Thus, these highly exothermic reactions could possibly results in a temperature runway and in an extensive sintering at a temperature where the rates of the reactions are significant. The rate of decomposition was reported to accelerate at around 270 °C and almost 80% of the nitrate rapidly decomposed at this temperature within a matter of seconds [18,31,44]. Failure to remove the heat release during this decomposition step caused sudden temperature runway in the catalyst bed to as high as 800 °C. This occurred in a matter of second for pure nickel nitrate [18]. A theoretical calculation based on a simple heat balance equation as follows, resulted in a bed temperature rise close to 1700 °C with zero flow rate of the reduction gas.

$$m^{\mathrm{Alum}} C_{\mathrm{p}}^{\mathrm{Alum}} \frac{dT_s}{dt} = r_{\mathrm{NO_3}} \Delta H_R - hA(T_s - T_g) \quad (9)$$

where T_s stands for the surface temperature of the support particles (K), T_g represents the temperature of the reducing gases (K), t denotes time (s), m^{Alum} corresponds to the mass of the support (kg) and $C_{\mathrm{p}}^{\mathrm{Alum}}$ stands for the specific heat capacity of the support (J/kg K). $r_{\mathrm{NO_3}}$ represents the rate of nitrate decomposition (kg/s) and ΔH_R stands for the overall heat of reaction (J/kg). h is for heat transfer coefficient (J/s m^2 K) and A is the area available for heat transfer (m^2).

The temperature increment was found to be around 450–500 °C in case of HMF. This is analogous to the DTA analysis of supported $Ni(NO_3)_2{\cdot}6H_2O$ by Bartholomew et al. [18], where the support functions as a heat sink. Nevertheless, the heat effect could be of major consequence in a large bed [18]. The very significant drop in surface area and collapse of porous structure as seen in the BET section in case of HMF serve as evidence in support of this statement. As the velocity of the reducing gas was increased as in the case of BF, there was a limited temperature increase, with the temperature remaining close to the oven temperature. The main reason for this variation is the availability of the heat transfer area. In case of HMF, the catalyst bed acted as a fixed bed composed of large cluster of particles resulted from channeling. However, with increasing velocity, the cluster size was reduced to smaller size exposing higher surface area for heat transfer. In case of BF, the cluster size was reduced to agglomerates of likely 2–5 particles. Thus, it resulted in maximum heat transfer from the reduction bed.

This theoretical observation has already been suggested by Bartholomew et al. [18] to minimize the sintering effect during decomposition of nitrate precursors. Results and discussions on the pore size distribution in Section 3.1 directly portray this detrimental effect of sintering over the prepared OCs. The reduced average crystal size reported in Table 2 also shows the favorable effect of high gas flow rate. High gas flows facilitates the transport processes and reduces the growth of Ni crystallites. This was shown by removing the water generated in decomposition steps as discussed already in Section 3.1. Similar decomposition behavior was also reported nitrate precursors for La [30] and Co [29].

This heat of reaction causes the sintering through dehydroxylation of the support. It has been shown by several authors [46–49] that at 500 °C, there is a complete removal of hydroxyls from the γ-Al_2O_3 100 facets. These hydroxyls are however, partially removed at this temperature from the γ-Al_2O_3 110 facets. γ-Al_2O_3 is a defective spinel phase of alumina with cation site vacancies randomly distributed throughout the crystal. Al ions occupy both the tetrahedral (25–37.5%) and octahedral sites [38,49–52]. The hydroxyl ions are a necessary component of the defect structure, their number being equal to the number of cation vacancies [49,51,52].

Due to the dehydroxylation of these surfaces, Al^{3+} at tetrahedral sites drop from the surface layer to the vacant interstices of the bulk structure to satisfy the valance requirements [49]. A surface Al^{3+} in a tetrahedral site is highly unstable. Thus, the reconstruction triggered by dehydroxylation of the (1 1 0) and (1 0 0) facets completely eliminates this unstable surface species [53]. This Spontaneous reconstruction completely depleted tetrahedral Al^{3+} reported in NMR studies [54]. Based on electron diffraction study Jayaram et al. [55] suggested that the γ → δ transformation begins with the ordering of tetrahedral cations in small (1–2 nm) domains. Rietveld analysis of diffraction spectra from several Al_2O_3 polymorphs suggests that the reduction of surface area and ordering of the tetrahedral aluminum sub-lattice, which occurs during heating, cause a gradual collapse of the cubic spinel framework. This allows, in the early stages of transformation, the structure to exhibit tetragonal character, being transformed later into the monoclinic θ-Al_2O_3 configuration [50]. Two important trends during cation ordering in the structural sequence from bohemite to θ-Al_2O_3 were outlined by Levin et al. [52]: (i) a gradual decrease in occupancy of the tetrahedral sites by aluminum cations, correlated with an increase in occupancy of the octahedral sites, and (ii) a gradual decrease in the total number of cation vacancies.

Based on the discussion above, it is apparent that in case of the HMF, there is reduced metal support interaction with inadequate heat removal from the large particle clusters. This causes the surface Al^{3+} atoms in tetrahedral configuration to migrate to the bulk. This leads to a collapse in the cubic spinel framework with reduction of specific surface area. Though, the surface temperature in this case is estimated to be around 500 °C, the core of the cluster could display an even much higher temperature. As a result the BET, TPR, XRD and the chemical properties of the surface of the support may, in this case, resemble those of θ-Al_2O_3, whereas the bulk may still in the γ- or δ-phase.

As the reducing gas velocity increases, this migration of Al^{3+} diminishes resulting in an increased metal support interaction. Thus, under the BF condition one can expect that the γ-Al_2O_3 structure is retained by most particles while under MF a mixture of δ- and γ-phases can be expected. Thus, the available bonding sites and especially the reducibility of nickel found to be higher on the mixture of aluminas, containing less OH-group (in other words less Al^{3+} atoms in tetrahedral configuration) than the pure γ-alumina [56].

Another purpose of this study was to determine the stability of the OC under repeated TPR/TPO cycles resembling the harsh operating condition of an industrial scale CLC plant. Most of the cases the OC lose its activity due to agglomeration of metal particles. Crystal agglomeration reduces the oxygen carrying capacity, thus the reducibility with each cycle. To investigate these, sequential reduction–oxidation as in cyclic TPR/TPO, H_2 chemisorption was performed in between each redox cycle.

Table 3 listed the f_{R} (%), D (%), d_v (nm) and f_{O} (%) for 10 cycles of operations. For all the samples, the sequence of TPR/TPO cycles demonstrates consistent percentage reduction of nickel, indicating that the samples are stable and that no phase transformation is taking place during the repeated cyclic redox process. The hydrogen pulse chemisorption results further confirmed the stability and reactivity of the sample in consecutive reduction and oxidation cycles. The reduction percentage is lower in case of HMF due to the reduced surface area and due to the collapse of porous structure of the support caused burial of nickel as discussed already in the BET

Table 3
Stability of OC (reduction, dispersion, crystal size and oxidation) over repeated TPR/TPO cycles.

Sample		TPR/TPO cycles									
		1	2	3	4	5	6	7	8	9	10
HMF	f_R	87	84	84	85	82	88	86	85	88	83
	D	1.58	1.70	1.76	1.65	1.62	1.71	1.68	1.50	1.65	1.51
	d_v	62.07	59.16	59.93	56.52	57.34	57.62	59.54	57.61	58.98	55.13
	f_O	77	79	79	78	79	79	78	78	77	79
MF	f_R	97	96	96	98	95	97	97	96	96	95
	D	1.97	1.95	2.17	1.92	2.13	2.04	2.17	2.01	2.01	1.91
	d_v	46.41	45.30	44.76	52.05	50.31	47.62	44.49	45.27	46.65	48.58
	f_O	83	83	83	82	85	84	83	85	83	84
BF	f_R	97	98	97	97	98	98	97	98	98	99
	D	3.91	3.74	3.84	3.78	3.86	3.77	3.88	3.90	4.00	3.81
	d_v	26.05	25.48	22.50	25.43	24.34	24.04	23.69	24.93	21.99	27.93
	f_O	86	86	86	85	86	86	86	87	87	85

section. On the other hand, high surface area facilitates accessibility to most of the nickel in case of MF and BF.

There is consistent smaller crystallite size for particles resulting from BF conditions suggesting the absence of agglomeration. However, the smaller particles in case of BF pretreatment could be the results of for strong metal support interactions, as shown in Fig. 4. Regarding this matter, Choi et al. [38] showed that the Ni particles on κ-Al_2O_3 were smaller than those on the γ-Al_2O_3. As mentioned, the γ-Al_2O_3 contains more acidic sites (Al^{3+} in tetrahedral configurations) that will interact with the Ni more strongly than the neutral κ-Al_2O_3. Based on the calculated Fermi level energy and Spacing between adjacent level of metal particles, Che et al. [57] reported that the physical and catalytic properties start to change near or below 2 nm of the metal particles. The surface energy created by non-saturated atoms in corner, edge, and plane sites becomes less significant with increasing Ni particle size greater than 1.94 nm [58]. Thus given the expected larger than 1.9–2 nm crystallite sizes, it is not the particle sizes but rather the availability of Al^{3+} in tetrahedral configurations and/or concentration of hydroxyl ion on the support surface that determines the reducibility and metal support interactions.

3.3. XRD

The X-ray diffractograms of γ-Al_2O_3 and the OCs in calcined and reduced forms are presented in Fig. 5 with the reference peaks from JCPDS. Diffraction peaks corresponding to crystalline species of either La_2O_3, $La(OH)_3$, $La_2(CO)_2O_2$ or $LaAlO_3$ phases were not detected indicating a well-dispersed, amorphous lanthanum phases on the surface of the support. In addition, no Co_3O_4, $CoAl_2O_4$ or $NiCo_2O_4$ peaks were also observed in the XRD patterns. This is understandably due to the low concentration of Co (1%) in the carrier material. However, the influence of replacing a relatively small fraction of Ni by an equivalent amount of Co in order to minimize the undesirable formation of aluminate [12], in all the three cases, has already been discussed in Section 3.2.

The major diffraction lines were observed at 2θ values of 37.3°, 43.3°, 63°, 75.5°, and 79.5°. These lines could be traced back to the bulk NiO crystal in all the three cases of calcined oxygen carriers. These lines were sharper and more intense for HMF and MF than for BF. This shows that larger nickel oxide particles were formed under HMF and MF conditions. On the other hand, in case of BF, a broad peak corresponds to well-dispersed small crystals on thin layer of amorphous nickel species were observed. Similar observation was reported by Heracleous et al. [59] for more than 15 wt% of Ni over γ-Al_2O_3. This suggests the saturation of the alumina surface by two-dimensional Ni species and the formation of multilayer/crystalline Ni phases. The monolayer dispersion capacity of NiO on Al_2O_3 has been reported to range from 13 to 20 wt% Ni loading. This has been determined by ion scattering spectroscopy [39], XRD [33] and XPS [60].

The average Ni crystal size in case of BF was found 5.2 nm using Eq. (3). The broadening of Ni (1 1 1) diffraction line for reduced OC was used to calculate the crystal size. For sample HMF and MF, Ni crystals were found 20.3 and 17.7 nm respectively. Though, smaller Ni crystals are found by XRD measurements compare to the crystal sizes obtained by H_2 pulse chemisorption experiments, the decreasing order of crystal sizes based on preparation methods shows similar results. XRD cannot detect crystals below 2–4 nm. On the other hand, H_2 chemisorption experiments account both the crystals and amorphous phase of Ni. Due to this, the crystal sizes measured by XRD differ from those obtained by H_2 pulse chemisorption experiments.

Based on the discussion in Section 3.2, one could also expect visible diffraction lines for $NiAl_2O_4$ and δ/θ-phase of alumina. To examine the presence of $NiAl_2O_4$, all the three OCs were reduced under H_2 flow at 750 °C before the XRD experiments. It is apparent from the TPR results that no $NiAl_2O_4$ got reduced below this temperature. As a result, if there were $NiAl_2O_4$ in crystalline from, one should expect a diffraction line at 2θ ~37°. However, the complete

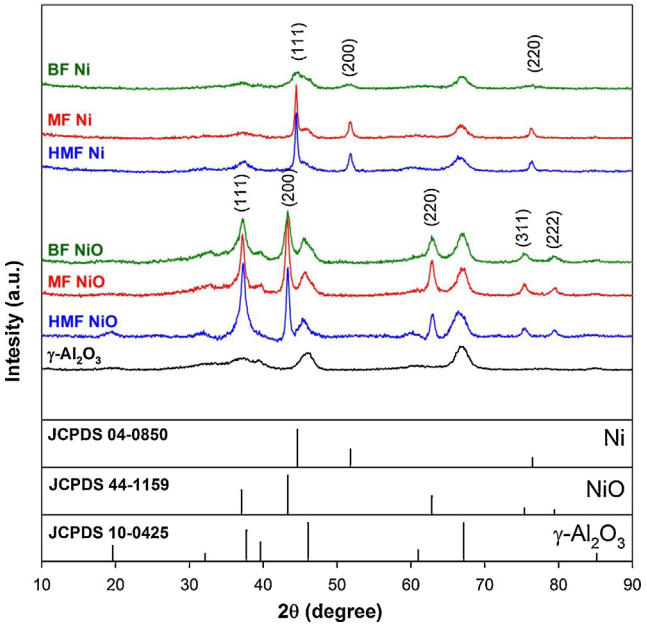

Fig. 5. XRD spectra of γ-Al_2O_3, calcined and reduced OC carrier. Reference peaks for γ-Al_2O_3, NiO and Ni are from JCPDS 10-0425, 44-1159 and 04-0850 respectively.

disappearance of NiO (1 1 1) diffraction line (Fig. 5) in all three reduced samples is suggesting of the absence of $NiAl_2O_4$ crystallites. Other strong diffraction lines of $NiAl_2O_4$ appear at 2θ 45°, 60° and 66°, which also could be present in case of all the three prepared oxygen carriers. However, γ-Al_2O_3 also provides diffraction lines in these 2θ values. Therefore, identification of such species is not very easy using XRD analysis, whereas their presence is easily detectable using TPR experiments. Bolt et al. [12] reported that such species exhibit structural, spectroscopic, and chemical similarities with bulk spinels but are not detectable with XRD.

Similar observations have been reported by several others [48,61,62] in characterization study of transition alumina (γ-, δ- or θ-Al_2O_3) surfaces by this well-established analytical technique. This is due to the intrinsic properties of these phases namely low crystallinity and small particle size. This bulk technique, however, is ineffective for the detection of molecularly thin surface layers that might possess structural properties (geometric, electronic, coordination) significantly different from those of the bulk. On the other hand, chemical probes (i.e., surface reactions TPR/TPO, TPD, chemisorptions etc.) provide important information useful for the inference of the changes in the near-surface structural properties of solid materials. The information gained from such studies can also be used to directly correlate catalytic properties with surface structure [48].

TPR study provides seemingly clear evidence for phase transformation of γ-Al_2O_3 to δ-phase for MF and θ-phase for HMF; however, these changes are not visible in Fig. 5. This phase transformation might occur at the interfaces between Ni crystallites and the alumina support surfaces, whereas the bulk structure of the support remained in the γ-phase. Transformation from γ to γ′ (an intermediate phase between γ and δ-Al_2O) occurs by dehydroxylation in the amorphous region rather than the crystal phase. This is accompanied by cation ordering by maintaining the ratio of tetrahedral and octahedral sites [61]. Kwak et al. [48] reported the possibilities of core-shell structure. The bulk of the alumina crystallites is phase-pure γ-Al_2O_3, whereas the surfaces of the particles have structures of the δ-Al_2O_3 [61] or θ-Al_2O_3 phase. These new phases are formed through dehydroxylation of the (1 0 0 and 1 1 0) facets of the γ-Al_2O_3. In a combined UV/visible Raman, XRD, and high-resolution TEM study similar conclusions were reported for TiO_2 phase transformation [62].

3.4. Analysis of reactivity at CREC Riser Simulator

All the three prepared OCs were investigated for the reactivity and stability under CLC fluidized bed conditions in the CREC Riser Simulator using methane for reduction cycles. The reduction reactions were carried out for 30 s at 650 °C under atmospheric condition. On the other hand, during the oxidation cycles, the reduced carrier was regenerated under air flow at 550 °C for at least 10 min to ensure complete oxidation of the carrier and combustion of any coke produced during reduction reaction.

In CLC, a high operating temperature (1000–1200 °C) is generally recommended to maximize the downstream turbine efficiency for power generation [1,5,63,64]. However, this increased efficiency comes at the expense of NO_x formation during the oxidation cycles and thus, eliminates one of the main advantages of CLC. Apart from this, a high operating temperature also facilitates metal sintering and agglomeration of OC particles. These morphological changes result in the reduced activity of the OC in successive cycles [36]. Therefore, CLC at a lower temperature range offers significant potential and implementation value [13,67]. This is why, the characteristic evaluation of the prepared OCs in this study was limited to a temperature of up to 950 °C (the highest temperature level of TPR/TPO experiments).

The chromatographic analysis of the exit gas from the CREC Riser Simulator's vacuum box identified CO_2 (35–37%) and H_2O (63–65%) as the major species with traces of H_2 (0.1–0.3%) and CO (0.9–0.7%) as the byproducts of the methane combustion reaction. Therefore, it is assumed that the reduction of the Ni based OCs proceeds mainly through the following combustion reaction:

$$CH_4 + 4NiO \rightarrow CO_2 + 2H_2O + 4Ni \quad (10)$$

$$CH_4 + NiO \rightarrow CO + 2H_2 + Ni \quad (11)$$

It is also important to highlight that though there are formations of CO and H_2 through non-catalytic solid–gas combustion processes (11), both of these gases are very reactive with the metal oxide under the studied reaction conditions [13,67,68]. On formation, these gases readily react with the existing metal oxide and are converted to CO_2 and H_2O according to the following combustion reactions:

$$CO + NiO \rightarrow CO_2 + Ni \quad (12)$$

$$H_2 + NiO \rightarrow H_2O + Ni \quad (13)$$

Therefore, OC favors the complete oxidation of CH_4 to CO_2 and H_2O at the beginning of the reduction process (or short contact times). Similar conclusions has been drawn by several others [69–71] based on pulse and continuous experiments in a batch fluidized reactor with Ni based OCs. As the reaction proceeds, there is evidence of contribution of reduced OC sites, which start catalyzing the following reactions:

Reforming:

$$CH_4 + H_2O \overset{Ni}{\longleftrightarrow} CO + 3H_2 \quad (14)$$

$$CH_4 + 2H_2O \overset{Ni}{\longleftrightarrow} CO_2 + 4H_2 \quad (15)$$

$$CH_4 + CO_2 \overset{Ni}{\longleftrightarrow} 2CO + 2H_2 \quad (16)$$

Water–gas shift:

$$CO + H_2O \overset{Ni}{\longleftrightarrow} CO_2 + H_2 \quad (17)$$

Decomposition:

$$CH_4 \overset{Ni}{\longleftrightarrow} C + 2H_2 \quad (18)$$

$$C + CO_2 \overset{Ni}{\longleftrightarrow} 2CO \quad (19)$$

$$C + H_2O \overset{Ni}{\longleftrightarrow} CO + H_2 \quad (20)$$

Based on the exit gas composition, it is believed that the water–gas shift reaction (17) mainly limits the conversion of CO and H_2 to CO_2 and H_2O at the operating temperature of this study. The water–gas shift is also reported to be relatively fast compared to other catalytic reactions [68]. Nonetheless, the reforming reactions (14–16) were also reported as relevant at the high operating temperatures of CLC. However, in this study, the contributions of these reactions were neglected because of the low reaction temperatures. Moreover, Iliuta et al. [67] reported that the decomposition reactions (18–20) were insignificant in the range of 600–950 °C and that carbon formation began only when the OC conversion is above 80%. This was also observed from the outlet gas analyses of the carrier re-oxidation cycle (regeneration) in the cases of all three prepared OCs. It is also believed that addition of La plays a great role in minimizing the carbon formation.

Thus, all these gas–solid catalytic reactions depend on the degree of the reduction of the OC [13,65,66,68]. In other words, reaction time strongly affects the extent of reduction and is a crucial controlling parameter. Careful manipulation of the contact time between the fuel and the OC could minimize the undesired side

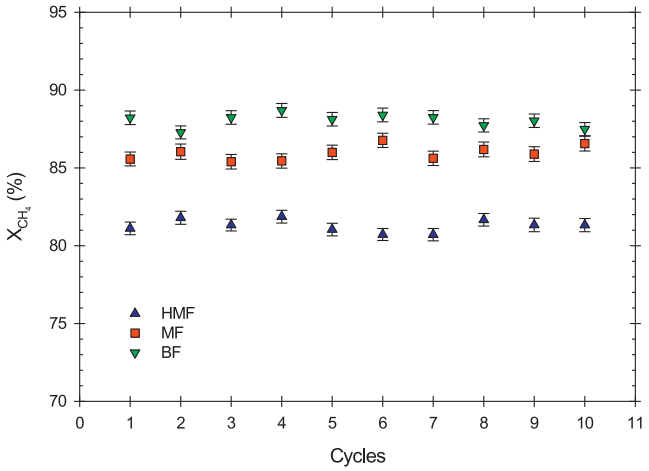

Fig. 6. Conversion of methane during multiple CLC cycles in CREC fluidized bed Riser Simulator (T: 650 °C, P: 1 atm, t: 30 s). Note: each cycle was reproducible within ± 2.5% standard deviation.

reactions at the cost of reduced CH_4 conversion, though complete combustion of methane is highly desirable in CLC.

Therefore, in this study, the CH_4 was allowed to react with 20% excess oxygen. Excess oxygen was calculated from reaction stoichiometry using expected OC's oxygen carrying capacity. For example, for 30 s reduction time, 6 mL CH_4 were injected for the HMF OC regenerated at 550 °C. These operating parameters resulted in a maximum CH_4 conversion with a negligible contribution from the gas–solid catalytic reactions. The CH_4 conversion was calculated using Eq. (4) and the results were plotted in Fig. 6

In the case of the OC prepared under HMF conditions, the X_{CH_4} was found to be 81.5%. Moreover, the OCs prepared under MF and BF conditions, showed an increased oxygen carrying capacity resulted in an increased X_{CH_4} to 86.3 and 88.4% respectively. This was the result of a both higher surface area and higher metal crystallite dispersion. Methane conversion results obtained with the OCs of this study displayed a ±2.5% standard deviation. This suggests that the prepared OCs are highly stable under multiple reduction and oxidation cycles. These findings also agreed with the results obtained from the physical and chemical characterizations, which confirmed high reactivity and stability of the OCs prepared in this study.

4. Conclusions

The followings are the concluding remarks of the present study:

i. The chemistry and careful control of the preparation steps significantly influence the desired physical and chemical properties of the OC. Controlled dehydroxylation as discussed in the BET and the TPR/TPO section was found to be beneficial in order to minimize the metal support interaction, increase the surface area and enhance the oxygen carrying capacity.
ii. The reducibility and structural properties of the OCs are indicative of the existence of δ- and θ-phase. However, their absence in the XRD experiments suggest that this phase transformation might occur at the interfaces between Ni crystallites and the alumina support surfaces, whereas the bulk structure of the support remained in the γ-phase.
iii. The three prepared OC showed excellent reactivity and stability under the high operating temperature of a CLC plant throughout the cyclic TPR/TPO experiments and in harsh fluidized bed conditions of the CREC Riser Simulator during the reduction runs with CH_4.
iv. The OC prepared under MF condition was found to be providing the best OC, based on surface area, dispersion, oxygen carrying capacity and reducibility below 750 °C of the sample.

References

[1] J. Adanez, A. Abad, F. García-Labiano, P. Gayan, L.F. de Diego, Progress in Energy and Combustion Science 38 (2011) 215–282.
[2] M. Ishida, D. Zheng, T. Akehata, Energy 12 (1987) 147–154.
[3] W.K. Lewis, E.R. Gilliland, M.P. Sweeney, Chemical Engineering Progress 47 (1951) 251–256.
[4] H.J. Richter, K.F. Knoche, ACS Symposium Series 235 (1983) 71–85.
[5] M.M. Hossain, H.I. de Lasa, Chemical Engineering Science 63 (2008) 4433–4451.
[6] P. Gayán, L.F. de Diego, F. García-Labiano, J. Adaĭnez, A. Abad, C. Dueso, Fuel 87 (2008) 2641–2650.
[7] P. Gayán, C. Dueso, A. Abad, J. Adánez, L.F. de Diego, F. García-Labiano, Fuel 88 (2009) 1016–1023.
[8] M.M. Hossain, H.I. de Lasa, Chemical Engineering Science 65 (2010) 98–106.
[9] K.E. Sedor, M.M. Hossain, H.I. de Lasa, Chemical Engineering Science 63 (2008) 2994–3007.
[10] C. Dueso, F. García-Labiano, J. Adánez, L.F. de Diego, P. Gayán, A. Abad, Fuel 88 (2009) 2357–2364.
[11] M.M. Hossain, H.I. de Lasa, AIChE Journal 53 (2007) 1817–1829.
[12] P.H. Bolt, F.H.P.M. Habraken, J.W. Geus, Journal of Solid State Chemistry 135 (1998) 59–69.
[13] M.M. Hossain, D. Lopez, J. Herrera, H.I. de Lasa, Catalysis Today 143 (2009) 179–186.
[14] M.M. Hossain, M.R. Quddus, H.I. de Lasa, Industrial and Engineering Chemistry Research 49 (2010) 11009–11017.
[15] J.W.C. Liberatori, R.U. Ribeiro, D. Zanchet, F.B. Noronha, J.M.C. Bueno, Applied Catalysis A 327 (2007) 197–204.
[16] M.C. Sanchez-Sanchez, R.M. Navarro, J.L.G. Fierro, Catalysis Today 129 (2007) 336–345.
[17] J. Xu, W. Zhou, Z. Li, J. Wang, J. Ma, International Journal of Hydrogen Energy 34 (2009) 6646–6654.
[18] C.H. Bartholomew, R.J. Farrauto, Journal of Catalysis 45 (1976) 41–53.
[19] H.I. de Lasa (1992).
[20] P.A. Webb, C. Orr, Analytical Method in Fine Particle Technology, 1st ed., Micromeritics Instrument Corp., 1997.
[21] S. Brunauer, L.S. Deming, W.E. Deming, E. Teller, Journal of the American Chemical Society 62 (1940) 1723–1732.
[22] J.H. De Boer, B.C. Lippens, Journal of Catalysis 3 (1964) 38–43.
[23] S. Lowell, J.E. Shields, M.A. Thomas, M. Thommes, Characterization of Porous Solids and Powders: Surface Area, Pore Size and Density (Particle Technology Series), Springer, 2004.
[24] J.H. De Boer, B.C. Lippens, B.G. Linsen, J.C.P. Broekhoff, A. van den Heuvel, T.J. Osinga, Journal of Colloid and Interface Science 21 (1966) 405–414.
[25] B.C. Lippens, B.G. Linsen, J.H. De Boer, Journal of Catalysis 3 (1964) 32–37.
[26] J.H. De Boer, A. van den Heuvel, B.G. Linsen, Journal of Catalysis 3 (1964) 268–273.
[27] C.H. Bartholomew, R.J. Farrauto, Fundamentals of Industrial Catalytic Processes, 2nd ed., John Wiley & Sons Inc., 2006.
[28] X. Chen, Y. Liu, G. Niu, Z. Yang, M. Bian, A. He, Applied Catalysis A 205 (2001) 159–172.
[29] C. Ehrhardt, M. Gjikaj, W. Brockner, Thermochimica Acta 432 (2005) 36–40.
[30] S. Mentus, D. Jelić, V. Grudić, Journal of Thermal Analysis and Calorimetry 90 (2007) 393–397.
[31] W. Brockner, C. Ehrhardt, M. Gjikaj, Thermochimica Acta 456 (2007) 64–68.
[32] C.H. Bartholomew, Catalysis Letters 7 (1990) 27–52.
[33] P.K. De Bokx, W.B.A. Wassenberg, J.W. Geus, Journal of Catalysis 104 (1987) 86–98.
[34] J.T. Richardson, M.V. Twigg, Applied Catalysis A 167 (1998) 57–64.
[35] J.T. Richardson, B. Turk, M.V. Twigg, Applied Catalysis A 148 (1996) 97–112.
[36] R. Villa, C. Cristiani, G. Groppi, L. Lietti, P. Forzatti, U. Cornaro, S. Rossini, Journal of Molecular Catalysis A: Chemical 204/205 (2003) 637–646.
[37] J.M. Rynkowski, T. Paryjczak, M. Lenik, Applied Catalysis A 106 (1993) 73–82.
[38] J. Choi, S. Zhang, J.M. Hill, Catalysis Science and Technology 2 (2012) 179.
[39] M. Wu, D.M. Hercules, Journal of Physical Chemistry 83 (1979) 2003–2008.
[40] F.-W. Chang, M.-S. Kuo, M.-T. Tsay, M.-C. Hsieh, Journal of Chemical Technology and Biotechnology 79 (2004) 691–699.
[41] K.V.R. Chary, P.V. Ramana Rao, V. Venkat Rao, Catalysis Communications 9 (2008) 886–893.
[42] R. Blom, I.M. Dahl, A. Slagtem, B. Sortland, E.T. Spjelkavik, Catalysis Today 21 (1994) 535–543.
[43] T. Mattisson, A. Järdnäs, A. Lyngfelt, Energy and Fuels 17 (2003) 643–651.
[44] B. Jang, M. Helleson, C. Shi, A. Rondinone, V. Schwartz, C. Liang, S. Overbury, Topics in Catalysis 49 (2008) 145–152.
[45] S. Yuvaraj, L. Fan-Yuan, C. Tsong-Huei, Y. Chuin-Tih, Journal of Physical Chemistry B 107 (2003) 1044–1047.
[46] M. Digne, P. Sautet, P. Raybaud, P. Euzen, H. Toulhoat, Journal of Catalysis 226 (2004) 54–68.
[47] J.H. Kwak, D. Mei, C.H.F. Peden, R. Rousseau, J. Szanyi, Catalysis Letters 141 (2011) 649–655.

[48] J.H. Kwak, C.H.F. Peden, J. Szanyi, Journal of Physical Chemistry C 115 (2011) 12575–12579.
[49] K. Sohlberg, S.J. Pennycook, S.T. Pantelides, Chemical Engineering Communications 181 (2000) 107–135.
[50] R.-S. Zhou, Ro.L. Snyder, Acta Crystallographica Section B: Structural Science 47 (1991) 617–630.
[51] J.A. Wang, X. Bokhimi, A. Morales, O. Novaro, T. López, R. Gómez, Journal of Physical Chemistry B 103 (1999) 299–303.
[52] I. Levin, D. Brandon, Journal of the American Ceramic Society 81 (1998) 1995–2012.
[53] J.M. McHale, A. Navrotsky, A.J. Perrotta, Journal of Physical Chemistry B 101 (1997) 603–613.
[54] D. Coster, A.L. Blumenfeld, J.J. Fripiat, Journal of Physical Chemistry 98 (1994) 6201–6211.
[55] V. Jayaram, C.G. Levi, Acta Metallurgica 37 (1989) 569–578.
[56] J.P. Jacobs, L.P. Lindfors, J.G.H. Reintjes, O. Jylha, H.H. Brongersma, Catalysis Letters 25 (1994) 315–324.
[57] M. Che, C.O. Bennett, Advances in Catalysis 36 (1989) 55–172.
[58] K. Kinoshita, Electrochemical Oxygen Technology, John Wiley & Sons, New York, 1992.
[59] E. Heracleous, A. Lee, K. Wilson, A. Lemonidou, Journal of Catalysis 231 (2005) 159–171.
[60] X. Wang, B. Zhao, D. Jiang, Y. Xie, Applied Catalysis A 188 (1999) 201–209.
[61] G. Paglia, C.E. Buckley, A.L. Rohl, R.D. Hart, K. Winter, A.J. Studer, B.A. Hunter, J.V. Hanna, Chemistry of Materials 16 (2004) 220–236.
[62] J. Zhang, M. Li, Z. Feng, J. Chen, C. Li, Journal of Physical Chemistry B 110 (2006) 927–935.
[63] J. Wolf, M. Anheden, J. Yan, Fuel 84 (2005) 993–1006.
[64] J. Wolf, J. Yan, International Journal of Energy Research (2005) 739–753.
[65] H. Jin, T. Okamoto, M. Ishida, Energy and Fuels 12 (1998) 1272–1277.
[66] J. Adánez, F. García-Labiano, L.F. de Diego, P. Gayán, J. Celaya, A. Abad, Industrial and Engineering Chemistry Research 45 (2006) 2617–2625.
[67] I. Iluita, R. Tahoces, G.S. Patience, S. Rifflart, F. Luck, AIChE Journal 56 (2010) 1063–1079.
[68] M. Ortiz, L.F. de Diego, A. Abad, F. Garcia-Labiano, P. Gayan, J. Adanez, Energy and Fuels 26 (2012) 791–800.
[69] M. Johansson, T. Mattisson, A. Lyngfelt, A. Abad, Fuel 87 (2008) 988–1001.
[70] C. Dueso, A. Abad, F. Garcia-Labiano, L.F. de Diego, P. Gayan, J. Adanez, A. Lyngfelt, Fuel 89 (2010) 3399–3409.
[71] E. Jerndal, T. Mattisson, I. Thijs, F. Snijkers, A. Lyngfelt, International Journal of Greenhouse Gas Control 4 (2010) 23–35.